Optimization and Modeling of Complete Removal of N-Compounds from Oil Cut Using Response Surface Methodology (RSM) by CuAlO₂/ZSM-12&35 as a New Photocatalyst

M. Rahmati[a], R. Fazaeli[a,*], M. Giahi Saravani[a] and R. Ghiasi[b]

[a]Department of Chemistry, South Tehran Branch, Islamic Azad University, Tehran, 11365-4435, Iran
[b]Department of Chemistry, East Tehran Branch, Islamic Azad University, Qiam Dasht, Tehran, 18735-136, Iran

(Received 9 April 2020, Accepted 18 June 2020)

In this study, immobilized $CuAlO_2$ onto the ZSM-12&35 composite was prepared and used as a photocatalyst to remove N-containing oil pollutants (carbazole) through advanced oxidation without the use of any oxidants. In this method, acetone is used as a reaction solvent that can be partially converted to fuel oxygenated compounds (octane enhancers) under an aldol condensation reaction. Photocatalyst characterization was performed using X-ray diffraction (XRD), Fourier-transform infrared (FTIR) spectroscopy, field emission scanning electron microscopy (FESEM), energy-dispersive X-ray spectroscopy (EDS), mapping, and BET/BJH (Brunauer-Emmett-Teller & Barrett-Joyner-Halenda) techniques. The effect of operating parameters (pollutant concentration, catalyst dosage, and pH of the solution) on the efficiency of carbazole removal (model oil) was investigated through the RSM methodology. The removal products are identified by the gas chromatography (GC-MS) technique. The results indicated complete elimination of carbazole under ultraviolet light (UV light), as well as due to using UV light, the in-situ formation of typical fuel oxygenated compounds under aldol condensation among solvent molecules. Accordingly, this new protocol can be utilized to refine fuel products accompanied by enhancing their octane numbers.The novelty of this work is the coexistence of ZSM-12 and ZSM-35 in the composite ZSM-12&35 resulted from the exertion of a remarkable synergistic effect on oil pollutants (carbazole) removal through advanced oxidation.

Keywords: Advanced oxidation, Carbazole, ZSM-12&35, Photocatalyst, Fuel oxygenates

INTTRODUCTION

Nitrogen-containing pollutants in some cuts of crude oil, like carbazole, quinoline, pyridine and indole in fossil fuels during burning cause problems such as pipeline blocking, rusting of the equipment, as well as production of nitrogen oxides NO_x, which are pollutants of the air and play a major role in acidic rains [1,2]. Nitrides in oil cuts are also responsible for the creation of photochemical smog and destruction of the ozone layer. Some nitrides, particularly carbazole and its derivatives are highly carcinogenic. Besides, the destruction rate of these nitrides is very slow, and therefore their potential damage to human health will remain for a long time [3]. Another problem caused by nitrogen compounds is that they cause poisoning of the catalyst through occupying active regions of absorption [4]. Generally, fuels consist of two main types of basic and non-basic nitrides. Basic nitrides include aniline, quinoline, and its derivatives, and non-basic nitrides include indole, carbazole, and its derivatives. Since basic nitrides are easily removed by acid-base reactions, most studies and investigations have focused on the nitrogen removal of non-basic nitrides especially, carbazole which is present around 60% in distillation products related to the middle distillation of the crude oil [5,6]. As a result, the industries and the oil industry in special, have looked for solutions to remove nitrogen from this oil cut. So far, the best dehydrogenation method used throughout the world has been

*Corresponding author. E-mail: r_fazaeli@azad.ac.ir

hydrodenitrogenation (HDN) in the presence of various catalysts [6] and experimental data have shown that these compounds would hardly be removed by the traditional (HDN) method [1,7]. Therefore, considering the reasons mentioned above, many efforts have been developed to find an appropriate alternative with a simple method and low costs [7].

So far, many oxidants and catalysts have been used, many of which are known as a good oxidative system. For example, catalytic oxidation of carbazole has been done using oil-soluble t-butyl hydroperoxide (TBHP) as oxidant, and molybdenum IV oxide (MoO_3/D751, MoO_3/Al_2O_3, MoO_3/D113) as catalyst. Among the catalysts used, the highest yield was obtained around 77.3% in the presence of MoO_3/Al_2O_3 catalyst [1].

In another study, Sibel zor and Bilge Budak investigated the effect of PAn and PAn / ZnO photocatalysts on 100% removal of dye under the UV visible light irradiation and lightless environments. In both conditions, PAn/ZnO was better for waste water treatment [8].

The importance of zeolites as adsorbents and heterogeneous catalysts is known well. In this regard, mesopore materials with nano-sized cavities making up a large volume of their structure as a free space are considered as appropriate materials having important features such as very high surface area, high permeability, good selectivity, and thermal and acoustic resistance. Due to these structural features, these materials are efficiently used as a catalyst, ion exchange, separator, sensor, and for energy generation, wastewater treatment, membrane and insulation materials [9,10]. There are more than 180 different types of zeolites previously recognized by the International Zeolite Association. Individual types of zeolites differ in terms of size of the channel and rings [10-13], connectivity channels, and the presence or lack of a cage at intersections of the channel or along the channel itself [14].

In addition to the acidity of zeolites, the size of the channels and their dimensionality influence activity and selectivity in the transformation and deformation of organic compounds [15.16]. The crystal size of zeolites is expected to have a significant effect on the conversion of aromatic hydrocarbons and also selectivity results [17,18]. There is a series of different structural types of zeolites with various

catalytic behaviors such as ZSM-5 (3-D channel structure with 10-ring channels) and SSZ-35 (1-D structure with 10-ring channels and 18-ring cages [19]) which are medium-pore zeolites, also the most commonly studied large-pore zeolites are mordenite (1-D structure), MCM-58 (1-D isostructural with 12-ring channels), ITQ-4 and SSZ-42 (with undulating 1-D 12-ring system with cages [20,21]), and zeolite Beta (3-D 12-ring channel system), MCM-68 (3-D 12-10-10-ring channel system [22]), and SSZ-33 (3-D 12-12-10-ring system [23]). So, it is reasonable to conclude that the structure-property relationship of a catalyst is a key factor for further improvement in efficiency and selectivity [24].

ZSM-12 (MTW) is a silica-rich zeolite consisting of a unique one-dimensional 12-membered ring channel system with unique pore openings of 5.7 Å $\times$ 6.1 Å [25]. Because its pore size is slightly higher than the ZSM-5, it can be used to selectively convert large molecules, which cannot easily penetrate into the MFI framework. Besides, since ZSM-12 has acidic properties, it has been recommended as a useful catalyst in many reactions such as isomerization [26], hydroisomerization [23], and hydrocracking [28]. The ZSM-35 belongs to FER topology consisting of a two-dimensional intersection channel system, namely the 10-MR (0.42 $\times$ 0.54 nm) and 8-MR (0.35 nm) channels [29]. It has been widely used in catalytic processes such as hydrocarbon cracking and skeletal isomerization of n-olefins to iso-olefins. Generally, zeolites with a single structure are applied directly. However, in some cases, mixed or composite zeolites are preferred because of their specific performance [30]. For example, ZSM-5/ZSM-11 composite, a crystalline zeolite showed a high selective and sustained activity for the alkylation reaction with diluted ethylene [31].

Fuel oxygenates are chemical structures containing an oxygen part, generally, alcohols and ethers, which are usually utilized as fuel additives to enhance gasoline octane number. The use of oxygenated additives such as methyl tert-butyl ether (MTBE) has been shown to enhance after discarding lead-containing octane additive that led to the reduction of air pollution [32].

In this study, to improve the quality of the catalytic activity, a meso-composite ZSM-12&35 was synthesized aimed at showing a higher catalytic activity compared to
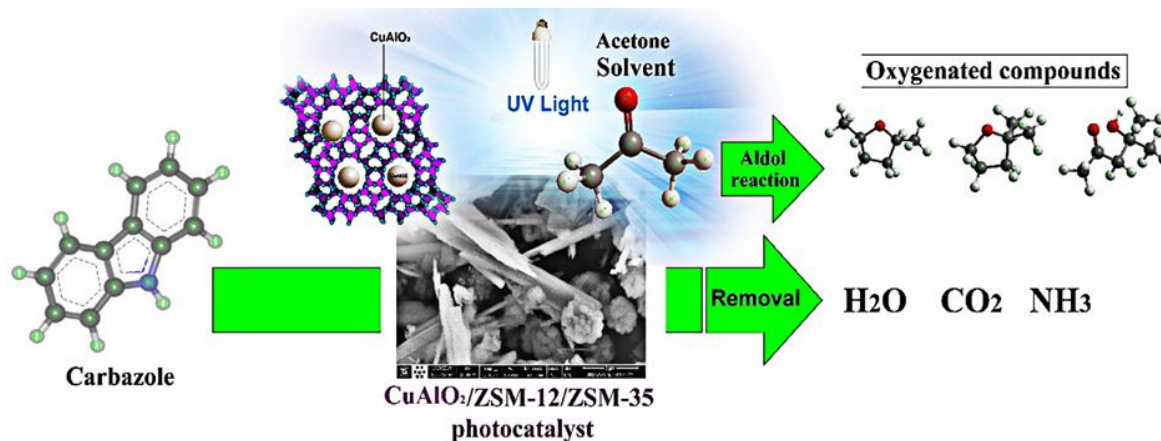
Scheme 1. Proposed pathways of carbazole and carbazole solvent photodegradation over CuAlO2/ZSM-12&35 under UV irradiation

any other pure zeolites. This composite can be formed from co-growth of ZSM-35 and ZSM-12 layers [29]. For removing and oxidizing of nitrogen compounds in the oil cuts, copper aluminate nanoparticles were used to modify the material in the cavity on immobilized ZSM-12&35 *composite*. Also, in this method, acetone is used as carbazole solvent that can be partially converted to fuel oxygenated compounds (octane enhancers) through aldol condensation reaction (Scheme 1). It is expected that using this method to a large extent can be useful in saving energy and catalyst production costs as well as in-situ production of oxygenated compounds in the process. In contrast to HDN methods, by using zeolite membranes for removal, the fuel value of the compounds reduces, and fuel oil value is maintained. Besides, the use of clean, environmentally friendly synthesis methods is the ultimate objective of this study.

MATERIALS AND METHODS

Materials

Hexamethyleneimine (HMI), silicic acid (H_4O_4Si), sodium aluminate (Al_2O_3 55%-Na_2O 45%), ammonium nitrate (NH_4NO_3), copper (II) acetate [$Cu(CH_3COO)_2$], carbazole($C_{12}H_9N$), acetone [$(CH_3)_2CO$], and other chemicals used were purchased from Sigma-Aldrich and Merck companies and used without any purification.

Characterization

Reactions were monitored by the thin-layer chromatography (TLC) (0.2 mm thickness, Merck) and the ultraviolet (UV) spectrophotometer. FT-IR patterns were prepared by the Brukers̀ VRTEX 70 FT-IR spectrophotometer using KBr disks. To characterize the synthesized heterogeneous catalysts, the XRD of the samples was scanned by a Holland Philips X-Pert X-ray Powder diffractometer using a Cu source with a peak Kα of 0.1540 nm from an angle of 1° to 100° scans. The FESEM model FESEM-TESCAN MIRA3 was used to determine morphology, surface properties, and also images of the catalyst surface. The (BELSORP Mini II) model was used to measure the specific surface area of the samples by the BET analyzer and also pore size distribution was studied using the BJH by adsorbing nitrogen at liquid nitrogen temperature.

Design of Experiments (DOE)

To design the test and perform the experimental design, the RSM and the DX software version 11 was used, respectively. The effect of pH, copper (copper aluminate), pollutant (carbazole) concentration, and composite mass on removal rate of carbazole was investigated. As the materials and their composition for removal have three different levels, so the BBD (Box-Behnken-Design) technique was used, that is able to control all blocks made by the

interactions of the levels [33].

To evaluate the effects of confounding variables on carbazole removal, initial values were obtained for operational factors using valid articles of the world standard. After performing preliminary tests, the confidence interval was determined for each of the variables, and the software introduced the confidence interval of each variable. At the pH range of 3-11, an amount of copper acetate salt with concentration of 0.01 to 0.4 M for copper aluminate loaded in the composition of the composite, the concentration of 2 to 32 mg l^{-1} of contaminating solution of carbazole, and nanocomposite mass of 0.004 to 0.12 g were determined. After entering declared numbers into the test design software, the suggested test pattern was obtained. After designing the experiment by the software, the experiments were carried out according to the table of Design of Experiments (Table 1).

Preparation of ZSM-12&35 Composite

The ZSM-12&35 composite was prepared from the ZSM-12&35 precursor named ZSM-12&35P according to previously reported methods of US patent [34] with some modifications. Accordingly, the synthetic mixture was obtained by mixing 3.74 g of $NaAlO_2$, 3 ml of 50% NaOH, and 20 ml H_2O under extreme stirring. Then, 10 ml of HMI was added dropwise to the reaction mixture in 30 min under the same stirring condition followed by the addition of silicic acid (46.76 g) slowly for at least 3 h with the lowest amount of water. The synthesized gel was transferred into a Teflon-lined autoclave which was sealed and placed on a Magnetic Stirrer-Heater for 36 h at 45 °C and then was transmitted to an oven and was heated at 160 °C for 12 days. The obtained wet cake was washed with deionized water. Chemical composition of the final wet cake was as follows:

$$0.11Na_2O \cdot 1.54Al_2O_3 \cdot 29.9SiO_2 \cdot 9.9H_2O$$
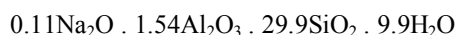
and in the next step, the resulting gel was transferred to the furnace at 540 °C.

The obtained solid from this step was refluxed with 375 ml NH_4NO_3 (2M) for two times successively for 6 h. The synthesized sample was named ZSM-12&35 composite.

Preparation of CuAlO$_2$/ZSM-12&35 Nanocomposite

A certain amount of synthesized mesoporous ZSM was dispersed in 100 ml of the aqueous solution containing 2 M copper acetate monohydrate and was stirred for 24 h at room temperature. Then, the achieved suspension was centrifuged at 12000 rpm for 10 min. The obtained solid was washed with deionized water and was allowed to dry at 100 °C for 3 h, then it was calcined at 450 °C for 12 h.

Removal Studies

Removal of nitrogenous compounds from the oil cut was carried out using photocatalytic CuAlO$_2$/ZSM-12&35 nanocomposites. In this study, the carbazole (petroleum shear model or oil cut model) was selected as the pollutant with a maximum absorption wavelength of 325 nm. Under a general procedure to remove the carbazole pollutants, 0.008 g of different nanocomposites was added to 20 ml of 2 mg l^{-1} of carbazole solution, and they were stirred at room temperature by a magnetic stirrer for 40 min. To investigate the performance of the nanocatalyst, the photocatalytic process was used in UV light in an optical reactor equipped with a (UV-C) mercury Philips 9W lamp. The pH of the suspensions was adjusted using 0.2 M NaOH and HCl, and efficiency was also calculated according to Eq. (1).

$$Efficiency\% = \frac{A_0 - A}{A} \times 100 \tag{1}$$

where A_0 and A are carbazole adsorption values at t = 0 and t = t, respectively.

To optimize the effect of nanocomposite concentration on the oxidative removal, different parameters such as the amount of synthetic CuAlO$_2$/ZSM12&3 (0.004, 0.006, 0.008, 0.01 and 0.12 g), solution pH (3, 7 and 11), and concentration of carbazole (2, 17 and 32 mg l^{-1}) were investigated. Notably, the experiments were performed in terms of the table of Design of Experiments (Table 1).

According to Table 1:

1. The carbazole solutions in the acetone solvent were prepared by the specified concentrations, 25 ml of each solution in a BG Bottle.

2. The pH of the carbazole solutions was adjusted using 0.2 M NaOH and HCl

3.   The different amounts of synthetic CuAlO$_2$/ZSM12&3 were added to BG Bottles containing carbazole solvent that were immediately transferred to the reactor and stirred for 40 min at room temperature by a magnetic stirrer.

4.   The reactions were monitored by the thin-layer chromatography (TLC) (0.2 mm thickness, Merck) and the ultraviolet (UV) spectrophotometer.

RESULTS AND DISCUSSIONS

XRD Analysis

The crystalline phase of the catalysts (ZSM-12&35 and CuAlO$_2$/ZSM-12&35) was analyzed by XRD with Cu-Kα radiation (λ = 0.154 nm) operating at 40 kV and 30 mA and was shown in Fig. 1.

Crystallinity was determined according to the sum of the three extreme reflections (2θ = 9.2°, 23.2° and 25.7°) [29,30]. Also, the crystallite size of the samples was calculated using the Scherrer equation [Eq. (2)],

$$D = \frac{K\lambda}{\beta\cos\theta} \tag{2}$$

where D is the average of crystallite size, k is crystal constant that is equal to 0.89, θ is the Bragg angle, λ is X-ray wavelength, and β is full width at half maximum of the strongest peak.

According to Eq. (2), the crystallite size was estimated between 44.8 and 91.5 nm, and the average crystallite size of the particles was equal to 69.48 nm.

Since XRD analysis is a suitable tool for proving the crystallinity and structure of the zeolites, therefore, the connection between stability and activity of the CuAlO$_2$/ZSM-12&35 nanocomposite was evaluated by XRD crystallization. Results showed that the crystallite size was between 13.73 and 44.88 nm, and the average of the particles was evaluated as *ca*. 30.95 nm. The index peaks indicated at the XRD pattern show that the CuAlO$_2$ is loaded onto the ZSM-12&35 [35].

The crystal size of CuAlO$_2$ was calculated as 26.84 nm using Eq. (2) at 2θ = 15.53°. This phase can be formed on the surface of zeolite acting as the semiconductor. It seems

that the amount of CuAlO$_2$ phase in the zeolite matrix was negligible due to the low-intensity index peaks.

FESEM and EDS Analyses

Figure 2 presents the results obtained from the FESEM and EDS analyses of the zeolite, indicating the agglomerated structure of ZSM-12&35 with a primary nanoparticle size between 45 and 91 nm. Comparing FESEM images of raw zeolite and composite samples, it was observed that zeolite particles contain much smaller nanoparticles than raw zeolite particles, though the morphology is almost the same. Elemental analysis of the sample was done by EDS analysis. Percentages of Si, N, Al, C and O are shown in EDS spectra for ZSM-12&35.

Figure 3 shows the results obtained from FESEM and EDS analyses of the CuAlO$_2$/ZSM-12&35 nanocomposite zeolite. The FESEM images showed two morphologies of zeolite structure formed from the composite matrix related to ZSM-12&35. The highest distribution is related to oxygen, and the lowest one belongs to copper. The EDS analysis indicated 0.74 wt% for Cu element in the zeolite composite. The lack of copper in this model is attributed to its very low loading.

X-Ray Mapping Analysis

Figure 4 shows the distribution of different elements on the surface of the crystalline lattice in the form of mapping patterns. The presence of Cu distributed at the surface of zeolite was shown in a map of CuAlO$_2$/ZSM-12&35.

FTIR Analysis

Figure 5 shows the FTIR spectra of the synthesized zeolites. There were no differences between the two spectrums, indicating the amount of copper in the zeolite matrix was negligible, and no prominent peaks were observed for CuAlO$_2$. Several peaks related to Si-O, Al-O, C-H, NO$_3^-$ and OH bonds were observed in both pictures that are attributed to the zeolite structure.

BET/BJH Analysis

Figure 6 presents the N$_2$ adsorption/desorption isotherms of ZSM-12&35 and CuAlO$_2$/ZSM-12&35. As shown in Fig. 6, functionalized ZSM-12&35 has a narrower

Table 1. Designing Experiments to Investigate the Effect of Variables on the Removal of Carbazole

Run	pH	Cu(CH₃COO)₂ concentration (M)	Pollutant concentration (mg l⁻¹)	Nanocomposite (g)	Removal (%)
1	3	0.205	32	0.006	42.18
2	7	0.205	17	0.120	96.76
3	7	0.205	17	0.120	-19.09
4	3	0.205	2	0.004	-37.50
5	7	0.400	32	0.120	-55.04
6	7	0.400	2	0.01	-250.00
7	3	0.400	17	0.004	31.68
8	11	0.010	17	0.006	-47.00
9	7	0.205	17	0.004	31.06
10	7	0.010	2	0.006	-359.09
11	7	0.400	32	0.004	34.10
12	7	0.205	17	0.006	1.29
13	11	0.205	2	0.120	87.50
14	11	0.010	17	0.004	7.92
15	7	0.010	32	0.120	56.58
16	7	0.010	32	0.008	-27.90
17	11	0.400	17	0.008	19.30
18	3	0.010	17	0.01	-50.99
19	11	0.205	32	0.120	100.00
20	7	0.205	17	0.120	9.38
21	7	0.400	2	0.006	-118.18
22	7	0.205	17	0.008	-4.20
23	7	0.010	2	0.004	-168.18
24	3	0.010	17	0.120	51.48
25	11	0.205	2	0.008	70.83
26	3	0.40	17	0.006	6.93
27	7	0.205	17	0.008	37.54

Table 1. Continued

28	3	0.205	32	0.120	-3.79
29	7	0.205	17	0.004	34.30
30	7	0.205	17	0.008	29.12
31	7	0.205	17	0.006	17.47
32	3	0.400	17	0.008	-51.48
33	7	0.010	2	0.008	-386.36
34	11	0.400	17	0.004	11.38
35	7	0.400	2	0.120	-100.00
36	3	0.205	32	0.004	-2.84
37	7	0.400	2	0.004	27.27
38	3	0.010	17	0.004	-52.97
39	7	0.010	32	0.006	-17.82
40	7	0.205	17	0.006	72.81
41	3	0.205	2	0.010	-241.66
42	7	0.400	2	0.008	-150.00
43	7	0.205	17	0.010	28.80
44	11	0.205	2	0.006	-100.00
45	3	0.205	2	0.120	0.00
46	7	0.010	2	0.120	163.63
47	7	0.205	17	0.004	64.72
48	11	0.205	32	0.006	14.69
49	7	0.400	32	0.008	16.27
50	7	0.400	32	0.006	84.49
51	3	0.205	32	0.010	77.72
52	11	0.205	32	0.010	9.95
53	7	0.205	17	0.010	19.74
54	7	0.205	17	0.010	21.35
55	11	0.205	2	0.010	-83.33
56	7	0.205	17	0.008	35.59
57	11	0.400	17	0.006	96.53

Table 1. Continued

58	7	0.010	2	0.010	-354.54
59	11	0.400	17	0.120	102.97
60	7	0.205	17	0.004	10.35
61	11	0.205	2	0.004	20.83
62	11	0.010	17	0.120	100.99
63	3	0.400	17	0.120	-12.87
64	11	0.010	17	0.008	86.13
65	11	0.205	32	0.008	46.44
66	3	0.400	17	0.010	-33.66
67	7	0.205	17	0.008	17.15
68	11	0.010	17	0.010	-45.54
69	3	0.010	17	0.006	-15.34
70	7	0.205	17	0.010	35.59
71	7	0.010	32	0.010	-81.39
72	7	0.010	32	0.004	60.40
73	7	0.205	17	0.006	62.78
74	7	0.205	17	0.010	70.87
75	3	0.205	2	0.008	-204.16
76	7	0.205	17	0.004	-18.40
77	7	0.205	17	0.120	36.31
78	7	0.400	32	0.010	39.33
79	7	0.205	17	0.006	-10.94
80	11	0.205	32	0.004	6.16
81	3	0.205	2	0.006	-220.83
82	11	0.400	17	0.010	-15.34
83	7	0.205	17	0.120	70.14
84	3	0.010	17	0.008	-45.04
85	3	0.205	32	0.008	14.21
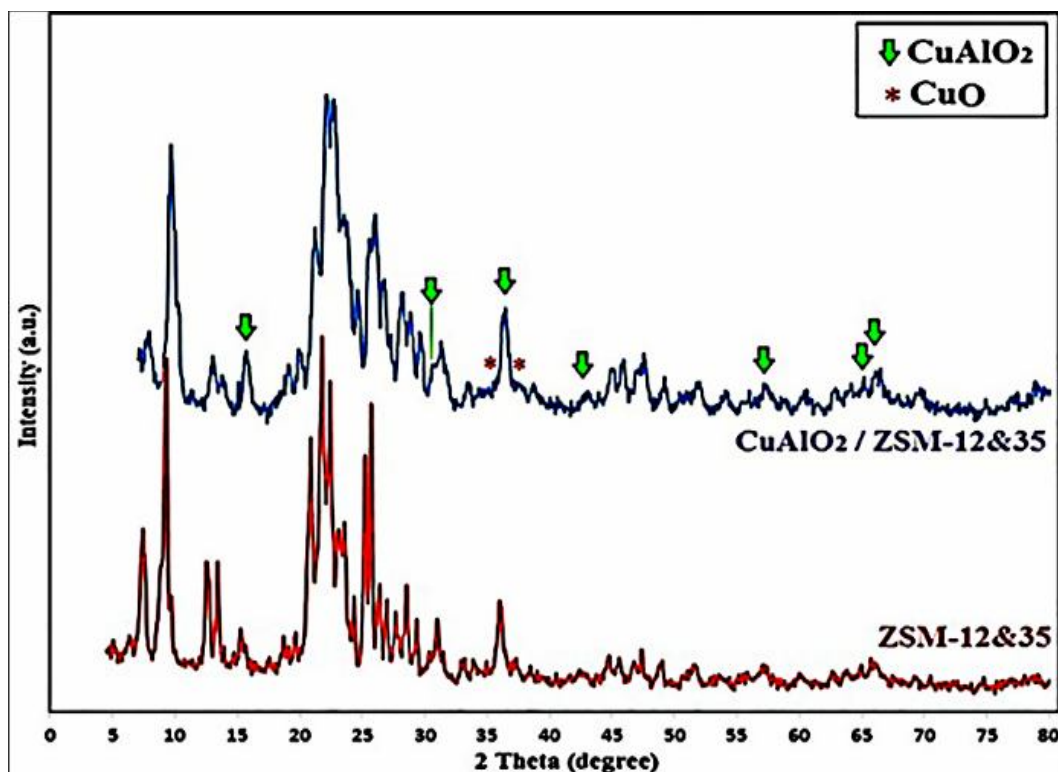
Fig. 1. The XRD patterns of the synthesized zeolites.

or smaller pore diameter and a smaller adsorption volume corresponding to the result obtained by XRD (Fig. 1).

Using BET, surface and pore diameter were also determined for ZSM-12&35 and CuAlO$_2$/ZSM-12&35. The BET analysis of ZSM-12&35 showed an area of 5.7535 [m^2 g^{-1}] and a pore volume of 0.026922 [cm^3 g^{-1}]. Since the surface area of the ZSM-12 is much larger than that of ZSM-35, the BET level of the MCM-12&35 mechanical mixture appears to be increased according to the ZSM-12 content. Functionalization of ZSM-12&35 (CuAlO$_2$/ZSM-12&35) resulted in reduced surface area (4.0437 [m^2 g^{-1}]) and pore volume (0.051736 [cm^3 g^{-1}]) . The specific pore volume, a surface area determined by the BET method, and average pore diameter obtained by the BJH method to functionalize ZSM-12&35 were found to decrease by increasing loaded material onto the surface of ZSM-12&35, as shown in Table 2.

Wall thicknesses of ZSM-12&35 and CuAlO$_2$/ZSM-12&35 were calculated based on Eq. (3).

$$Wall\ thickness = \frac{2d_{100}}{\sqrt{3}} - D_{BJH} \tag{3}$$

where 2d$_{100}$ is 2θ with the Bragg angle, and D$_{BJH}$ is pore diameter obtained by the B$_{JH}$ method (nm).

ZSM-12&35 sample exhibited type-IV N$_2$ isotherms with a hysteresis loop, confirming the simultaneous presence of micropores and meso/macropores in the obtained ZSM-12&35 product. The isotherm of the samples at low partial pressure (less than 0.1) showed high adsorption, indicating the presence of micropores in the samples, while hysteresis loop present in the region of 0.45 < P/P0 < 0.95 was found to be consistent with capillary density in mesopores and also could be due to structural defects or relative pressure of intercrystalline mesopores [36-38].

Removal Process

Figure 7 shows the results obtained from the reaction
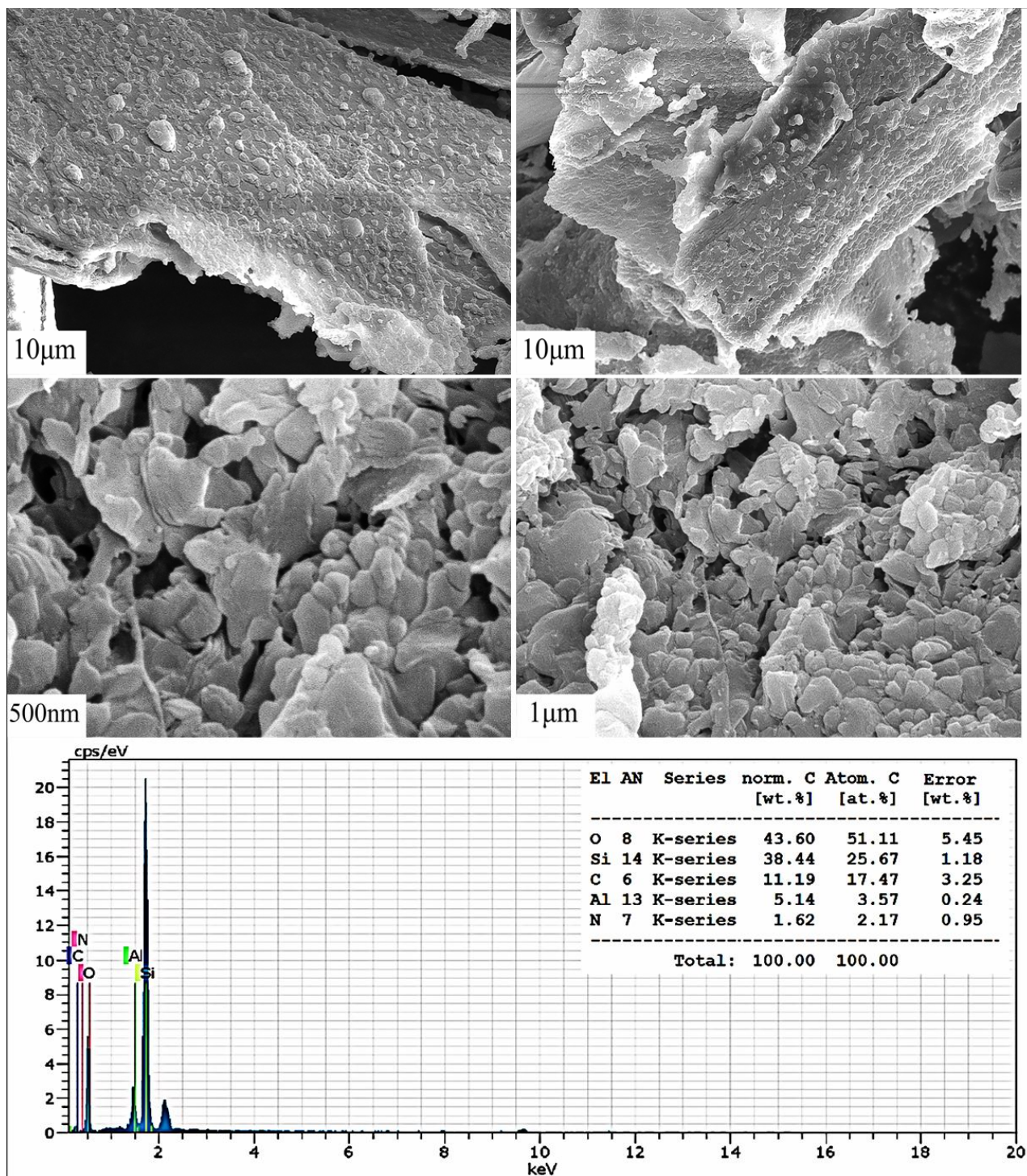
Fig. 2. FESEM images and EDS spectrum of ZSM-12&35.
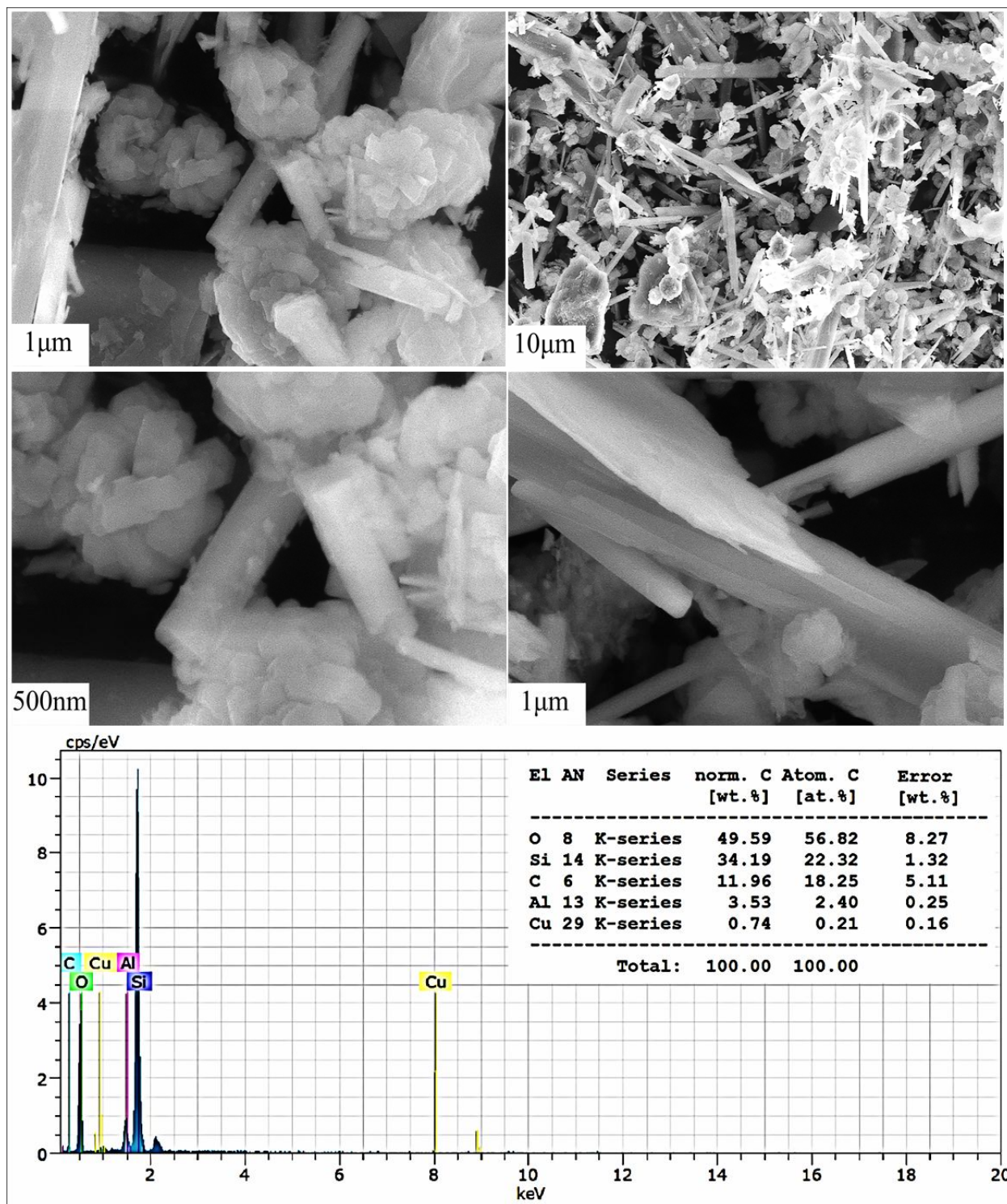
Fig. 3. FESEM images and EDS spectrum of CuAlO$_2$/ZSM-12&35.
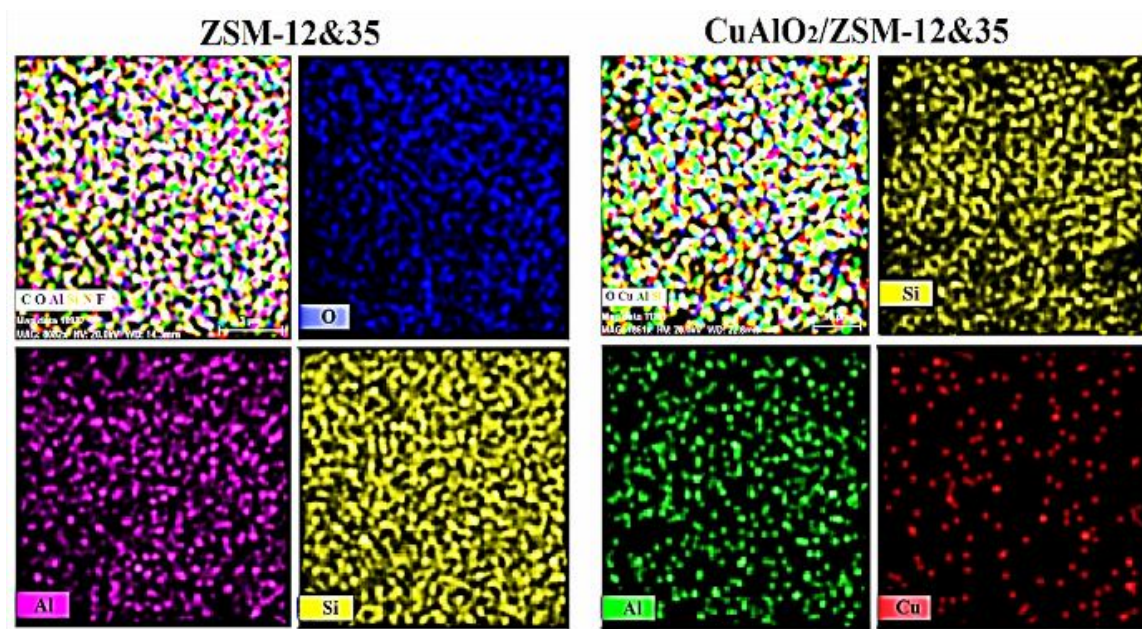
Fig. 4. X-ray mapping patterns of ZSM-12&35 and CuAlO$_2$/ZSM-12&35.
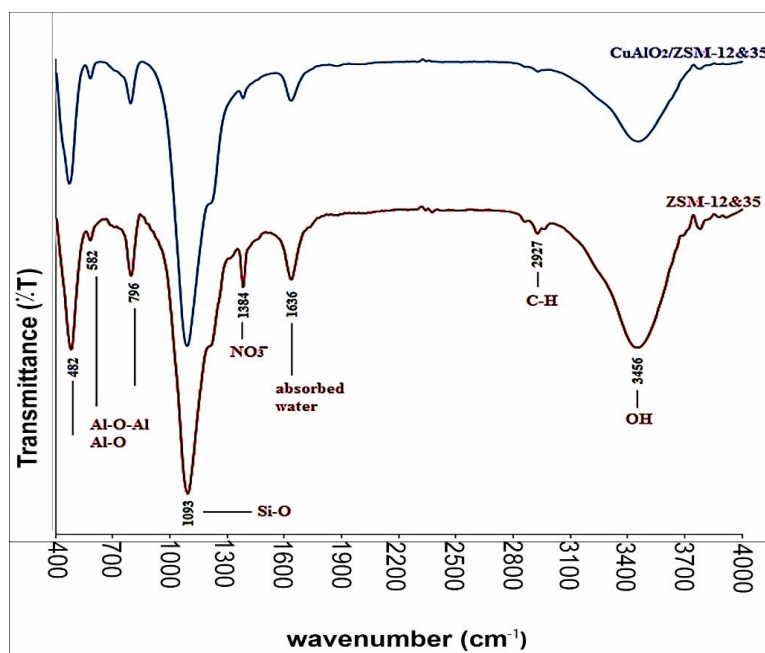
**Fig. 5.** FTIR spectra of ZSM-12&35 and CuAlO$_2$/ZSM-12&35.
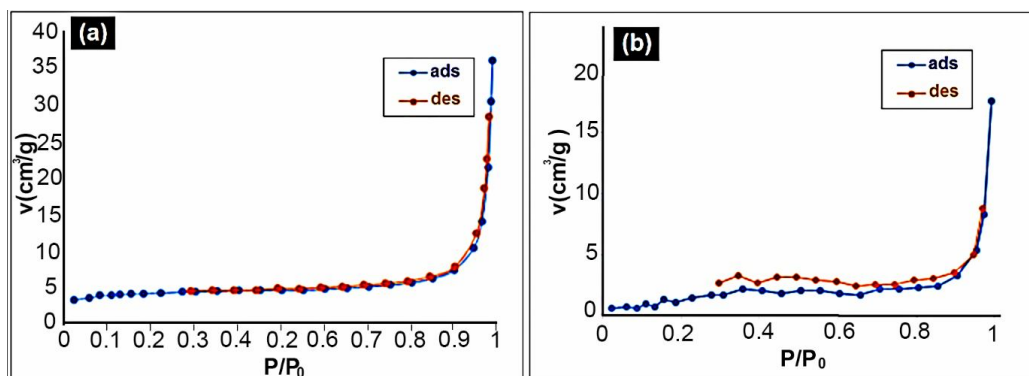
Fig. 6. Adsorption/desorption isotherm of a) CuAlO$_2$/ZSM-12&35 and b) ZSM-12&35.
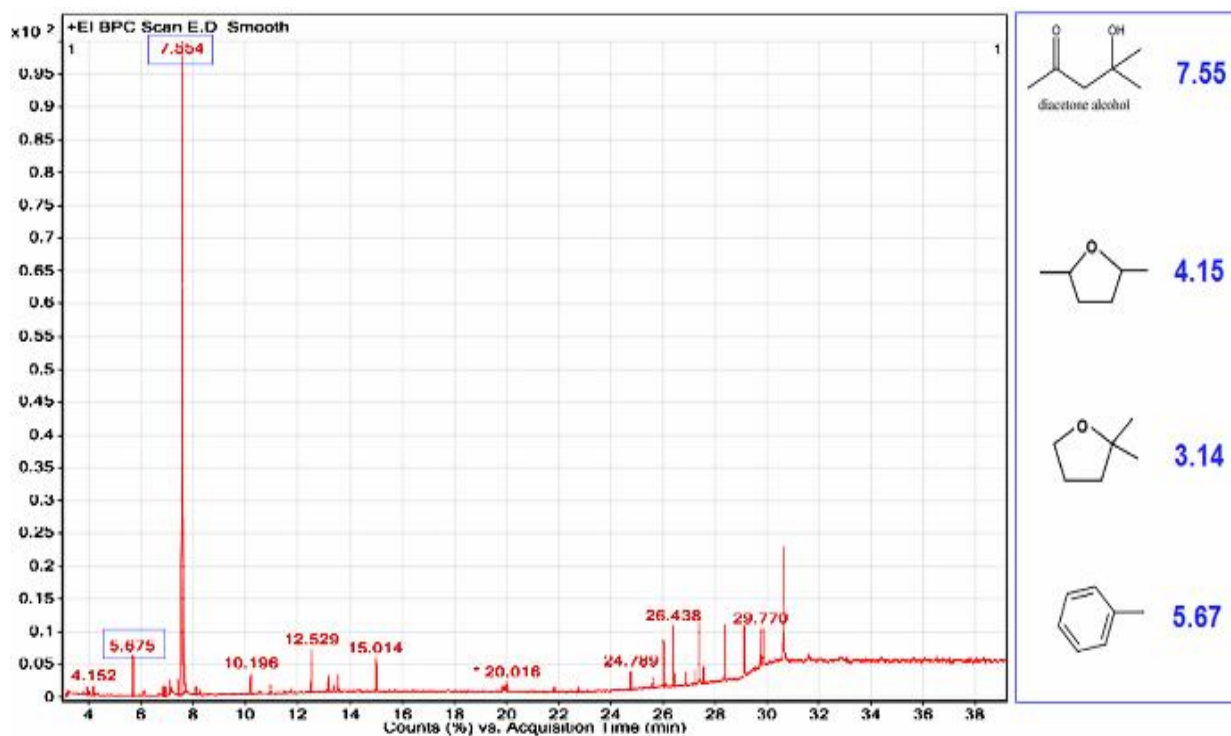
Fig. 7. GC-Mass chromatogram for test number 6.

Table 2. Textural Parameters Deduced from the Nitrogen Sorption Isotherm

Sample	S$_{BET}$ (m^2 g^{-1})	Pore diameter by B$_{JH}$ method (nm)	Pore volume (cm^3 g^{-1})	Wall diameter (nm)
ZSM-12&35	5.7535	1.21	0.026922	2.92
CuAlO$_2$/ZSM-12&35	4.0437	1.21	0.051736	3.18

mixture of test 6 from Table 1, taken by the catalyst under UV irradiation.

The carbazole peak was almost zero, indicating its complete elimination by a photocatalytic degradation reaction. The peaks that appeared in the spectrum included two categories of reaction products and noise device products resulting from previous contamination of the device column. Products in the reaction mixture are displayed in the right direction of the spectrum. The molecules observed at t = 7.55, 4.15 and 3.14 are generally attributed to the Aldol condensation reaction between acetone solvent in the presence of $CuAlO_2$ catalysts; the mechanisms of which are shown in Fig. 8.

Statistical analysis. $CuAlO_2$ phase, as an activator, catalyzes the Aldol condensation reaction between the two ketones (acetone solvent) from which ether cyclic compounds can be achieved by removing water and reducing it. The catalyst used has an integral potential for the conduction of the aldol reaction, which is very important in the production of organic compounds. Using the acetone solvent in this process (Fig. 8) led to the formation of three oxygenated molecules that can be used as octane enhancers such as MTBE in fuel products [39]. In fact, this method can be used for the removal of N-containing oil pollutants accompanied by in-situ formation of octane enhancers.

For carbazole, it can be said that almost complete destruction has occurred as well as the conversion of carbazole to volatile compounds such as CO_2 and NH_3. Toluene is the only molecule produced as a result of degradation, whose possible mechanism is illustrated in Fig. 9.

In addition to the complete removal of the carbazole pollutant, the results obtained from GC-MS observations showed a major peak at the time of 5.67, which is related to toluene with a λ range of 240-320 nm, and also showed that the catalyst effect on solvent has led to the development of new products at times of 7:55, 4:15 and 3:14, including 2,5-dimethylhydrofuran, 2,2-dimethylhydrofuran and MTBE, which have the λ range between 185-220 nm. Accordingly, they are out of our expectation; however, they are considered as desirable and in agreement with the removal of carbazole, which has led to the optimization of cut oil under Aldol reaction. The by-products resulted from the

carbazole removal reaction have the UV-λ_{max} or absorption peak in the same area as the carbazole UV-λ_{max}, as mentioned in valid scientific studies [40-41]. The tester cannot detect new products from the pollutant, and the absorption peak does not decrease after the degradation of carbazole. Also, under the Aldol reaction and based on the results, a part of the solvent was involved in the reaction. Therefore, the solvent volume decreased and the concentration of the solution increased, and consequently, the absorption peak rate increased, so the negative percentage results can be due to these points [42]. On the other hand, percentages of removal more than 100 in some cases of test results may indicate the removal of some by-products associated with carbazole pollutants.

As shown in Table 1, the highest percentage of removal of carbazole belongs to test 59, as obtained by 102%. Since test 62 has almost the same parameters and conditions with the test 59, it can be concluded that decreasing the amount of $CuAlO_2$ also reduces the removal of the oxidation capacity of the pollutant (carbazole and new by-products). Also, at first sight on Table 1, it can be concluded that all the variables in the experiment need to be aligned and balanced in order to optimize the elimination process. This replication and balance will be observed based on the output of statistical results as well as an optimal version by the BBD method and created blocks.

Considering the validity of the test less than 0.05 (0.0001) in the designed RSM model, as shown in Table 3, there is a significant difference between the effect of variables on elimination or oxidization of carbazole.

Therefore, it can be concluded that pH, copper, and pollutant concentration variables and also the amount of nanocomposite have a significant effect on the removal of carbazole. Also, since the test statistic of F in the pollutant concentration has exceeded the statistical value of the model, so it has had the greatest effect on the elimination of pollutants. It should be noted that the pH significance level was more than that of nanocomposite and copper aluminate content, showing that if these three variables are compared with each other, pH value has the greatest effect on the amount of removal of carbazole. Mathematical model of experimental design is as follows [Eqs. ((4)-(8))]:
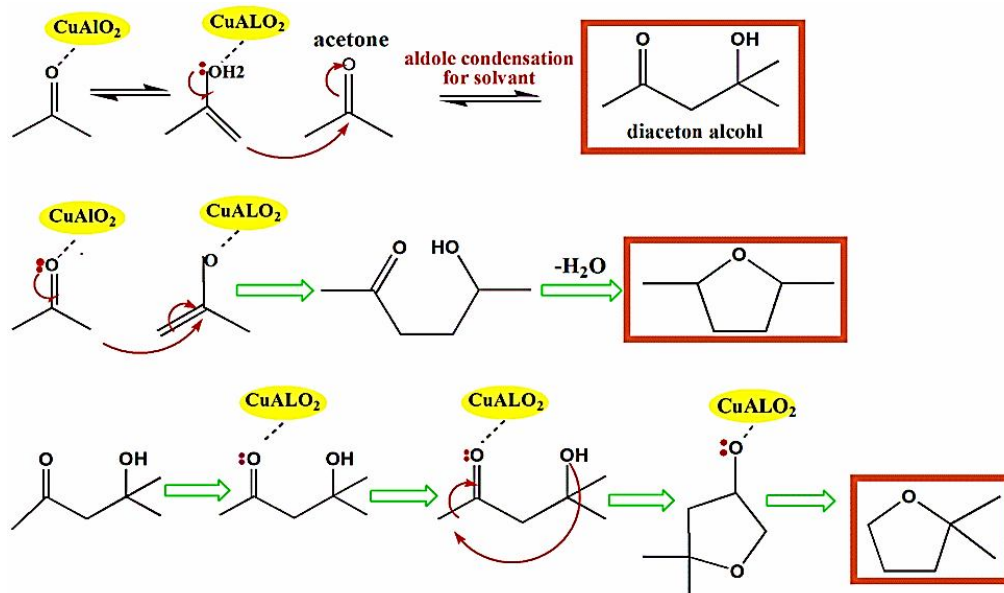
Fig. 8. Mechanism1: Aldol condensation reaction between acetone solvents in the presence of $CuAlO_2$.
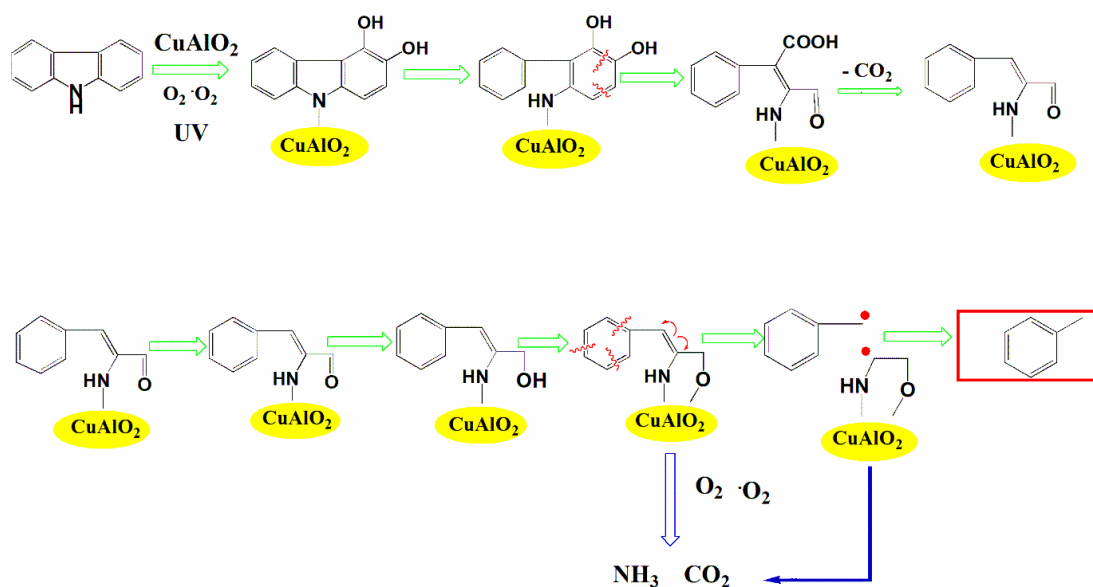

Fig. 9. Mechanism 2: destruction of carbazole and conversation to NH_3, CO_2 and toluene.

Removal (composite 0.004) = -265.829 + 19.4891 × [pH] + 848.047 × [Cu] + 10.3883 × [Pollutant concentration] + -26.0218 × [pH] × [Cu] + -0.205536 × [pH] × [Pollutant concentration] + -18.9582 × [Cu] × [Pollutant concentration] + -0.520547 × $[pH]^2$ + -435.906 × $[Cu]^2$ + -0.0863003 × $[Pollutant \ concentration]^2$ (4)

Removal (composite 0.006) = -396.721 + -0.719842 × [pH] + 552.486 × [Cu] + 30.1198 × [Pollutant concentration] + 38.8741 × [pH] × [Cu] + -0.618006 × [pH] × [Pollutant concentration] + -11.8447 × [Cu] × [Pollutant concentration] + -0.570273 × $[pH]^2$ + -724.177 × $[Cu]^2$ + -0.461331 × $[Pollutant \ concentration]^2$ (5)

Removal (composite 0.008) = -465.762 + -5.80458 × [pH] + 1300.46 × [Cu] + 30.0704 × [Pollutant concentration] + -19.3577 × [pH] × [Cu] + -1.01155 × [pH] × [Pollutant concentration] + -16.4254 × [Cu] × [Pollutant concentration] + 3.063 × $[pH]^2$ + -1836.22 × $[Cu]^2$ + -0.400967 × $[Pollutant concentration]^2$ (6)

Removal (composite 0.01) = -455.5 + 5.32928 × [pH] + 1060.45 × [Cu] + 31.05 × [Pollutant concentration] + 4.12541 × [pH] × [Cu] + -0.942108 × [pH] × [Pollutant concentration] + 1.38345 × [Cu] × [Pollutant concentration] + 0.958103 × $[pH]^2$ + -2287.73 × $[Cu]^2$ + -0.488601 × $[Pollutant concentration]^2$ (7)

Removal (composite 0.12) = 160.502 + -16.9293 × [pH] + -608.772 × [Cu] + -0.77843 × [Pollutant concentration] + 21.2617 × [pH] × [Cu] + 0.0678811 × [pH] × [Pollutant concentration] + 12.9922 × [Cu] × [Pollutant concentration] + 1.61155 × $[pH]^2$ + -101.136 × $[Cu]^2$ + -0.0824984 × $[Pollutant concentration]^2$ (8)

The normal probability graph shows how variables follow a normal distribution. When tested sample is more normal, the response can be obtained more accurate and more reasonable. As depicted in Fig. 10, the dispersion of the normal distribution of variables is linear. Since almost all the data is on a normal line, the statistical population of the data on the removal of the pollutants has a normal condition. Therefore, it can be concluded that the statistical population of carbazole pollutant removal data is normal. The normal state of the data indicates the accuracy and correct results by the user.

Box-Cox chart is a tool used to determine the most appropriate exponential transfer function to exert on the response (Fig. 11). The lowest point in the Box-Cox chart represents the best Lambda value where there is the least sum of created and remained squares in the converted model. When the ratio of maximum to minimum response is greater than 3, there will be a greater ability to improve the model using the exponential function.

Based on Fig. 11, in which the difference between minimum and maximum is equal to 3, thus no further exponential enhancement is considered for the experiment model. This chart also shows a 95% confidence interval.

According to Fig. 11, Lambda simulates the creation of a mathematical arithmetic link between the variables, in which current and actual values are determined, and the best point is presented for simulating and optimizing the experiments 1.8

3.6.2. Identifying variables' behavior on the removal of carbazole pollutant

By analyzing the three-dimensional graphs obtained from the experiments, the status of the effect of variables and their behavior in the experiment can be observed. As shown in Fig. 12, it is quite obvious that the interaction of substances at points of maximum alkali and maximum amount of $CuAlO_2$ reaches a reasonable effect. In other words, both of these two variables can simultaneously improve the effect of the removal of pollutants.

The green portion of Fig. 12 having a sharp drop, predicted under the software by default, confirms this hypothesis. If the amount of pH and $CuAlO_2$ decreases, as a result, no pollutants are removed. Even in actual amount, when the environment is acidic, not only the pollutant will not be eliminated, but also it will begin to interfere with the type of contamination spread in the environment.

As illustrated in Fig. 13, the removal of carbazole is also influenced by the increase in the pollutant content, but an important point in this section is the correlation between pH and pollutant concentration. As shown in the green section of Fig. 13, by increasing the amount of pH, removal was observed in all the amounts of pollutants. It is also most effective in matching pH variable with the amount of pollutant concentration in the alkaline environment at approximately 11, as shown in the upper yellow part of Fig. 13.

As shown in Fig. 14, the behavior of the two influential variables is clearly evident in the experiments. According to Table 3, pollutant concentration has the greatest effect on the removal of carbazole, which according to Fig. 14, it can be realized that this effect occurs simultaneously with the increase in the molar amount of loaded copper aluminate on the nanocomposites.

Isotherms Calculations

Using the data obtained from the tests, all the adsorption isotherms of a monolayer were calculated [43]. Table 4 presents the best isotherms in terms of error minimization

Table 3. ANOVA Analysis was Performed to Remove or Oxidize Carbazole

| ANOVA response surface methodology cubic model						
Source	Sum of squares	df	Mean square	F-value	p-value	
Model	7.994E+05	49	16314.01	6.63	<0.0001	Significant
A-pH	38400.76	1	38400.76	15.62	0.0004	
B-Cu	16351.39	1	16351.39	6.65	0.0143	
C-Pollutant Concentration	1.985E+05	1	1.985E+05	80.71	<0.0001	
D-composite	85166.57	4	21291.64	8.66	< .0001	
AB	173.52	1	173.52	0.0706	0.7921	
AC	21140.41	1	21140.41	8.60	0.0059	
AD	15859.69	4	3964.92	1.61	0.1930	
BC	7387.30	1	7387.30	3.00	0.0919	
BD	62928.02	4	15732.01	6.40	0.0006	
CD	99656.81	4	24914.20	10.13	<0.0001	
A^2	6960.92	1	6960.92	2.83	0.1014	
B^2	35310.49	1	35310.49	14.36	0.0006	
C^2	98456.83	1	98456.83	40.04	<0.0001	
ABD	7205.47	4	1801.37	0.7325	0.5760	
ACD	12549.68	4	3137.42	1.28	0.2981	
BCD	24789.29	4	6197.32	2.52	0.0586	
A^2D	7583.34	4	1895.83	0.7709	0.5515	
B^2D	21491.13	4	5372.78	2.18	0.0910	
C^2D	35104.83	4	8776.21	3.57	0.0153	
Residual	86072.70	35	2459.22			
Lack of fit	65225.72	15	4348.38	4.17	0.0018	Significant
Pure error	20846.98	20	1042.35			
Cor total	8.855E+05	84				
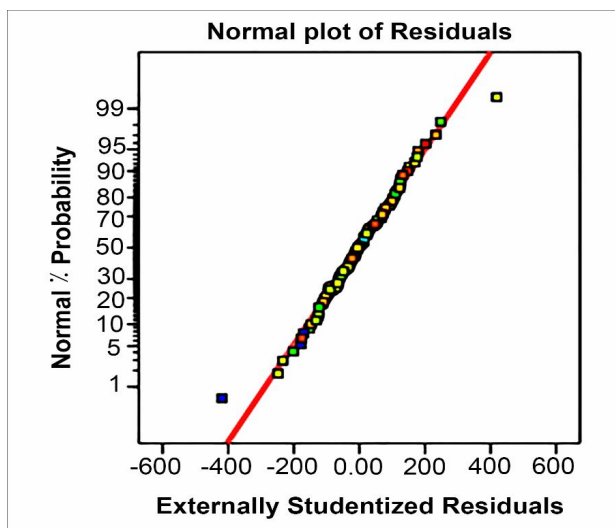
Fig. 10. Dispersion diagram of the normal distribution of the variables' response.
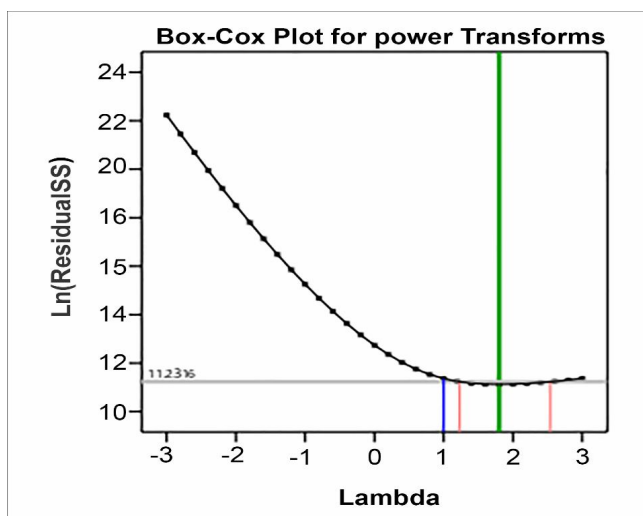

Fig. 11. BOX-COX chart (removal of carbazole).

Table 4. Optimal Condition for Carbazole Removing

| pH	$Cu(CH_3COO)_2$ Concentration (M)	Pollutant concentration	Composite	Removal & Aldol reaction	Desirability
9.5	0.03	6	0.12	131.425	1.000
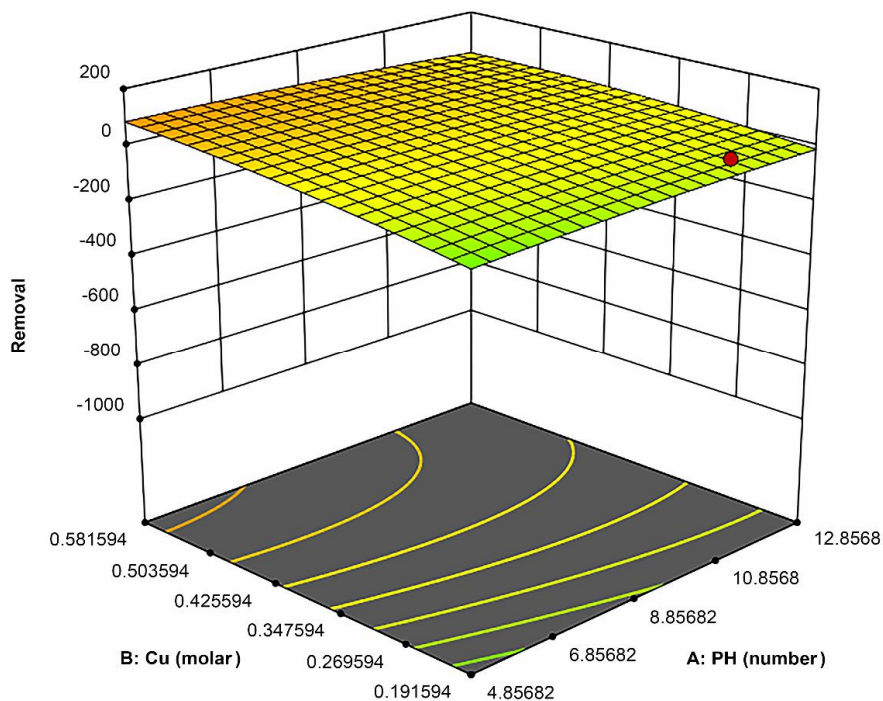
Fig. 12. Three-dimensional diagram of the relationships and variable effects of pH and copper oxide on the removal of carbazole.
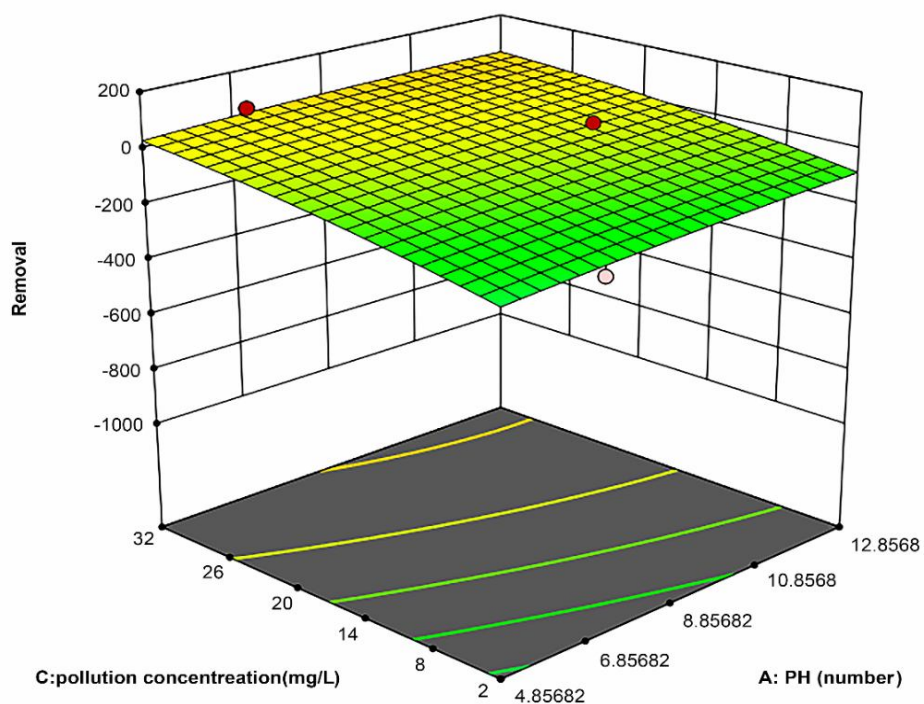

Fig. 13. Three-dimensional graph of the relationships and the variables effect of pH and the amount of pollutant concentration on the removal of carbazole.
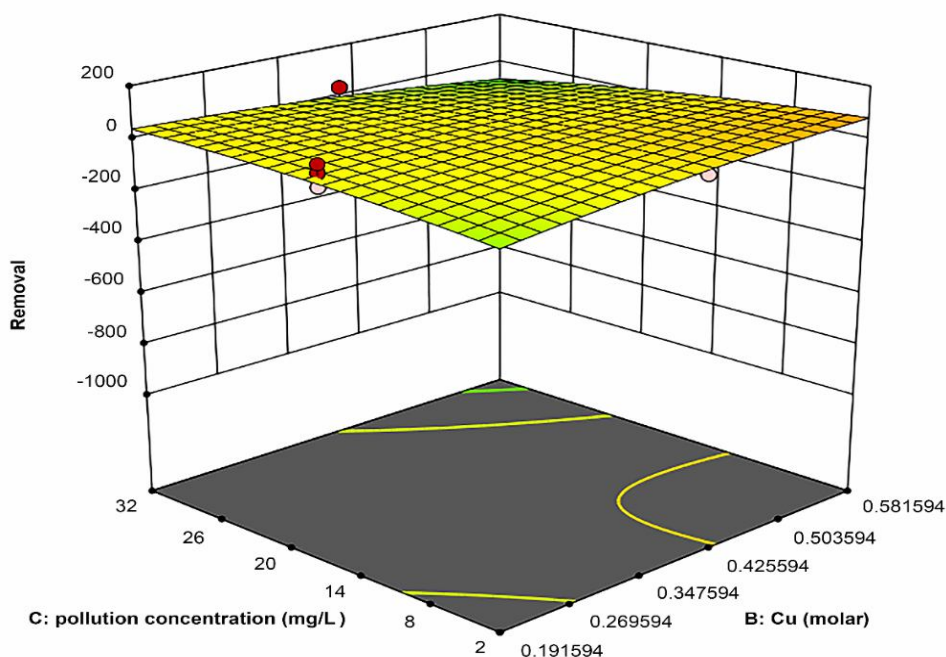
Fig. 14. Three-dimensional diagram of the relationships and the variable effects of copper oxide and the amount of pollutant concentration on the removal of carbazole.

and maximum correlation.

Accordingly, the Weber_Van_Vliet isotherm equation (the best single-layer adsorption isotherm) was found to be in good agreement with the results of this study [Eq. (9)].

$$Weber - Vant - Vliet : C_e = P_1 . q_e^{(P_2 . P_3 + P_4)} \qquad (9)$$

Where Ce is the equilibrium concentration of adsorbate [mg l^{-1}], q$_e$ is equilibrium adsorption capacity of adsorbent [mg g^{-1}], P_1 is Weber-van Vliet constant, P$_2$ is Weber-van Vliet model exponent, P$_3$ is Weber-van Vliet model exponent, and P$_4$ is the Weber-van Vliet model exponent.

CONCLUSIONS

In this study, a series of ZSM-12&35 composites were synthesized successfully under conditions of 0.11Na$_2$O · 1.54O · Al$_2$O$_3$ · 29.9SiO$_2$ · 9.9H$_2$O. An intergrowth of some ZSM-12 and ZSM-35 layers was found in these composites. Synthesized ZSM-12&35 composite catalysts showed higher activity than pure ZSM-12 or pure ZSM-35 zeolite catalyst based on previous studies [29], possibly due to synergism of ZSM-35 and ZSM-12.

CuAlO$_2$ as an activator semiconductor was formed at the surface of the zeolite and photocatalyst removal process for carbazole. In this method, acetone is used as a carbazole solvent that can be partially converted to fuel oxygenates compounds (octane enhancers) through an aldol condensation reaction. Results indicated complete elimination of carbazole under mild conditions as well as in-situ formation of typical fuel oxygenated compounds through aldol condensation between solvent molecules. Thus, this new protocol can be utilized to refine fuel products accompanied by enhancing their octane numbers.

Elimination of carbazole from cut oil in the presence of nanocatalyst using the RSM method was studied. Using this method, the optimal condition was obtained with pollutant concentration (6 ppm), synthetic CuAlO$_2$/ZSM12&35 (0.12 g) of Cu(CH$_3$COO)$_2$ with concentration (0.03 M) and solution pH (9.5).

Table 5. Isotherms, Error Minimization and Correlation Maximization

No.	Model	Equation	Error function value	Correlation coefficient
1	Weber-Van-Vliet	$C_e = P_1 \cdot q_e^{(P_2 \cdot q_e^{P_3} + P)_4}$	1.55%	0.9947
2	Radke-prausnitz	$q_e = \dfrac{a_{rp} \cdot r_{RP} \cdot C_e}{1 + r_{RP} \cdot C_e^{B_{RP}}}$	1.747%	0.9940
3	Redlich-Peterson	$q_e = \dfrac{K_R \cdot C_e}{1 + a_R \cdot C_e^{g}}$	1.747%	0.9939
4	Toth	$q_e = \dfrac{q_{mT} \cdot C_e}{(a_T + C_e^{z})^{\frac{1}{z}}}$	1.758%	0.9938
5	Schlunder	$q_e = \dfrac{C \cdot C_e^{\alpha}}{1 + D \cdot C_e^{\beta}}$ $q_e = \dfrac{q_{mFS} \cdot K_{FS} \cdot C_e}{1 + q_{mFS} \cdot C_e^{m_{FS}}}$	2%	0.9946
6	Jovanovich	$q_e = q_{mJ} (1 - e^{KJC_e})$	2.4%	0.9939
7	Keller	$q_e = \dfrac{q_m \cdot a \cdot b \cdot C_e}{[1 + (b \cdot C_e)^a]^{\frac{1}{a}}}$	2.4%	0.9938
8	Sips	$q_e = \dfrac{k_S \cdot a_S \cdot C_e^{B_S}}{1 + a_S \cdot C_e^{B_S}}$	2.515%	0.9936
9	Langmuir	$q_e = \dfrac{q_{mLb} \cdot C_e}{1 + bc}$	2.57%	0.9934
10	Khan	$q_e = \dfrac{q_{SK} \cdot b_K \cdot C_e}{(1 + b_K \cdot C_e)^{a_K}}$	2..6%	0.994
11	Koble-Corrigan	$q_e = \dfrac{A \cdot C_e^{n}}{1 + B \cdot C_e^{n}}$	2..6%	0.9936
12	Hill-Debuer	$C_e = \dfrac{q_e}{b \cdot (q_m - q_e)} \cdot e^{\left(\frac{q_e}{q_m - q_e}\right)} \cdot e^{\left(\frac{-C \cdot q_e}{q_m}\right)}$	3.707%	0. 9954

1.   Based on the results obtained from GC-MS observations, the negative efficiency of carbazole degradation can be justified because of two reasons:
The by-products resulted from the carbazole removal reaction have the UV-λ_{max} or absorption peak in the same area as the carbazole UV-λ_{max}. Hence, the tester cannot detect new products from the pollutant, and the absorption peak does not decrease after the degradation of carbazole.
2.   Under the Aldol reaction, a part of the solvent was involved in the reaction. Therefore, the solvent volume decreased and the concentration of the solution increased. Accordingly, a set of absorption peaks resulted from these two processes shows the higher absorption peaks than the initial carbazole.

Finally, as shown in Table 5, the optimal version of the experiment was performed with the maximum amount of carbazole removal accompanied by in-situ formation of fuel oxygenated components under the Aldol reaction.

ACKNOWLEDGMENTS

REFERENCES

[1] Zhou, X. R.; Hong, M. A.; Fu, X. M.; Yao, C. B; Xiao, J. Q., Catalytic oxidation of carbazole using t-butyl hydroperoxide over molybdenum catalysts. *J. Fuel. Chem. Techno.* **2010**, *38*, 75-97, DOI: 10.1016/S1872-5813(10)60021-7.

[2] Sano, Y.; Choi, K. H.; Korai, Y.; Mochida, I., Effects of nitrogen and refractory sulfur species removal on the deep HDS of gas oil. *Appl. Catal. B Environ.* **2004**, *53*, 169-174, DOI: 10.1016/j.apcatb.2004.05.014.

[3] Jha, A. M.; Bharti, M. K., Mutagenic profiles of carbazole in the male germ cells of Swiss albino mice. *Mutat. Res-Fund. Mol. M.* **2002**, *500*, 97-101, DOI: 10.1016/S0027-5107(01)00303-7.

[4] Wu, Y. C.; Yang, X. F.; Hao, L., Improved oxygen optical sensing performance from Re(I) complex doped MCM-41 composite samples by incorporating oxadiazole ring into diamine ligand: Synthesis; characterization and sensing response. *Sens. Actuators. B. Chem.* **2017**, *244*, 1113-20, DOI: 10.1016/j.snb.2017.01.128.

[5] Jain, S. L.; Joseph, J.K.; Sain, B., Alumina supported MoO3: an efficient and recyclable catalyst for selective oxidation of tertiary nitrogen compounds to N-oxides using anhydrous TBHP as oxidant under mild reaction conditions. *Catal. Lett.* **2007**, *115*, 8-12, DOI: 10.1007/s10562-006-9011-7.

[6] Laska, U.; Frost, C. G.; Price, G. J.; Plucinski, P. K., Easy-separable magnetic nanoparticle-supported Pd catalysts: Kinetics; stability and catalyst re-use. *J. Catal.* **2009**, *268*, 318-28, DOI: 10.1016/j.jcat.2009.10.001.

[7] Anastas, P. T.; Kirchhoff, M. M.; Williamson, T. C., Catalysis as a foundational pillar of green chemistry. *Appl. Catal. A.* **2001**, *221*, 3-13, DOI: 10.1016/S0926-860X (01)00793-1.

[8] Zor, S.; Budak, B., Investigation of the effect of PAn and PAn/ZnO photocatalysts on 100% 3 degradation of Congo red under UV visible light irradiation and lightless environments. *Envir. Turk. J. Chem.* **2019**, *5*, 6, DOI: 10.3906/kim-1907-30.

[9] Rutkowska, M.; Díaz, U.; Palomares, A. E.; Chmielarz, L., Cu and Fe modified derivatives of 2D MWW-type zeolites (MCM-22.; ITQ-2 and MCM-36) as new catalysts for DeNOx process. *Appl. Catal., B.* **2015**, *168*, 531-9, DOI: 10.1016/j.apcatb.2015.01.016.

[10] Xie, W.; Zheng, Y.; Zhao, S.; Yang, J.; Liu, Y.; *et al.*, Selective oxidation of pyridine to Pyridine-N-oxide with hydrogen peroxide over Ti-MWW catalyst. *Catal. Today.* **2010**, *157*, 114-8, DOI: 10.1016/j.cattod.2010.02.045.

[11] Littke, A. F.; Dai, C.; Fu, G. C., Versatile catalysts for the Suzuki cross-coupling of arylboronic acids with aryl and vinyl halides and triflates under mild conditions. *J. Am. Chem. Soc.* **2000**, *122*, 4020-8, DOI: 10.1021/ja0002058.

[12] Patzke, G. R.; Krumeich, F.; Nesper. R., Oxidic nanotubes and nanorods-anisotropic modules for a future nanotechnology. *Angew. Chem., Int. Ed.* **2002**, *41*, 2446-61, DOI: org/10.1002/1521-3773(20020715)41:14<2446: AID-ANIE2446>3.0.CO;2-K.

[13] Corma, A., Inorganic solid acids and their use in acid-catalyzed hydrocarbon reactions. *Chem. Rev.* **1995**, *95*(3), 559-614, DOI: 10.1021/cr00035a006.

[14] Bhan, A.; Iglesia, E., A link between reactivity and local structure in acid catalysis on zeolites. *Acc. Chem. Res.* **2008**, *41*, 559-67, DOI: 10.1021/ar700181t.

[15] Cejka, J., Introduction to zeolite science and practice. Elsevier: 2007.

[16] Uguina, M. A.; Sotelo, J. L.; Serrano, D. P., Toluene disproportionation over ZSM-5 zeolite: Effects of crystal size; silicon-to-aluminum ratio, activation method and pelletization. *Appl. Catal.,* **1991**, *76*, 183-

98, DOI: 1016/0166-9834(91)80046-Y.

[17] Bregolato, M.; Bolis, V.; Busco, C.; Ugliengo, P.; Bordiga, S.; *et al.,* Methylation of phenol over high-silica beta zeolite: Effect of zeolite acidity and crystal size on catalyst behaviour. *J. Catal.* **2007**, *245*, 285-300, DOI: 10.1016/j.jcat.2006.10.024.

[18] Wagner, P.; Nakagawa, Y.; Lee, G. S.; Davis, M. E.; Elomari, S.; *et al.,* Guest/host relationships in the synthesis of the novel cage-based zeolites SSZ-35; SSZ-36; and SSZ-39. *J. Am. Chem. Soc.* **2000**, *122*, 263-73, DOI: 10.1021/ja990722u.

[19] Chen, C. Y.; Finger, L. W.; Medrud, R. C.; Kibby, C. L.; Crozier, P. A.; *et al.,* Synthesis, Structure, and Physicochemical and Catalytic Characterization of the Novel High-Silica Large-Pore Zeolite SSZ-42. *Chem. A. Eur. J.* **1998**, *4*, 1312-23, DOI: 10.1002/(SICI)1521-3765(19980710)4:7<1312: AID-CHEM1312>3.0.CO;2-K.

[20] Elangovan, S. P.; Ogura, M.; Ernst, S.; Hartmann, M.; Tontisirin, S.; *et al.,* A comparative study of zeolites SSZ-33 and MCM-68 for hydrocarbon trap applications. *Microporous Mesoporous Mater.* **2006**, *96*, 210-5, DOI: 1016/j.micromeso.2006.06.038.

[21] Žilková, N.; Bejblová, M.; Gil, B.; Zones, S. I.; Burton, A. W.; *et al.,* The role of the zeolite channel architecture and acidity on the activity and selectivity in aromatic transformations: The effect of zeolite cages in SSZ-35 zeolite. *J. Catal.* **2009**, *266*, 79-91, DOI: 10.1016/j.jcat.2009.05.017.

[22] Kustov, L.; Golubeva, V.; Korableva, A.; Anischenko, O.; Yegorushina, N.; *et al.,* Alkaline-modified ZSM-5 zeolite to control hydrocarbon cold-start emission. *Microporous Mesoporous Mater.* **2018**, *260*, 54-8. DOI: 10.1016/j.micromeso.2017.06.050.

[23] Patil, C. R.; Niphadkar, P. S.; Bokade, V. V.; Joshi, P. N., Esterification of levulinic acid to ethyl levulinate over bimodal micro-mesoporous H/BEA zeolite derivatives. *Catal. Commun.* **2014**, *43*, 188-91, DOI: 10.1016/j.catcom.2013.10.006.

[24] Wei, X.; Smirniotis, P. G., Development and characterization of mesoporosity in ZSM-12 by desilication. *Microporous Mesoporous Mater.* **2006**, *97*, 97-106, DOI: 10.1016/j.micromeso.2006.01.024.

[25] Martens, J. A.; Perez-Pariente, J.; Sastre, E.;

Corma, A.; Jacobs, P. A., Isomerization and disproportionation of m-xylene, selectivities induced by the void structure of the zeolite framework. *Appl. Catal.* **1988**, *45*, 85-101, DOI: 10.1016/S0166-9834(00)82395-7.

[26] Mehla, S.; Krishnamurthy, K. R.; Viswanathan, B.; John, M.; Niwate, Y.; *et al.,* n-Hexadecane hydroisomerization over Pt/ZSM-12, role of Si/Al ratio on product distribution. *J. Porous Mater.* **2013**, *20*, 1023-9, DOI: 10.1007/s10934-013-9682-6.

[27] Zhang, W.; Smirniotis, P. G., Effect of zeolite structure and acidity on the product selectivity and reaction mechanism forn-octane hydroisomerization and hydrocracking. *J. catal.* **1999**, *182*, 400-16, DOI: 10.1006/jcat.1998.2337.

[28] Meier, W. M.; Olson, D. H.; Baerlocher, C., Atlas of Zeolite Structure Types. Elsevier, 1996.

[29] Niu, X.; Song, Y.; Xie, S.; Liu, S.; Wang, Q.; Xu, L., Synthesis and catalytic reactivity of MCM-22/ZSM-35 composites for olefin aromatization. *Catal. Lett.* **2005**, *103*, 211-8, DOI: 10.1007/s10562-005-7156-4.

[30] Chen. H.; Shen. B.; Pan, H., *In situ* formation of ZSM-5 in NaY gel and characterization of ZSM-5/Y composite zeolite. *Catal. Lett.* **2003**, *32*, 726-7, Doi, 10.1246/cl.2003.726.

[31] Feng, X.; Zhang, P.; Fang, Y.; Charusiri, W.; Yao, J.; *et al.,* Designing a hierarchical nanosheet ZSM-35 zeolite to realize more efficient ethanol synthesis from dimethyl ether and syngas. *Catal. Today.* **2020**, *343*, 206-214, DOI: 10.1016/j.cattod.2019.02.054.

[32] Sanhoob, M. A.; Muraza, O.; Al-Mutairi, E. M.; Ullah, N., Role of crystal growth modifiers in the synthesis of ZSM-12 zeolite. *Adv. Powder Technol.* **2015**, *26*, 188-92, DOI: 10.1016/j.apt.2014.09.007.

[33] Zarrinabadi, E.; Abghari, R.; Nazari, A.; Mirjalili, M., Environmental effects of enhancement of mechanical and hydrophobic properties of polyester fabrics using silica/kaolinite/silver nanocomposite, a facile technique for synthesis and RSM optimization. *EurAsian J. Bio. Sci.* **2018**, *12*, 437-50.

[34] Fung, A. S.; Lawton, S. L.; Roth, W. J., Inventors, ExxonMobil Oil Corp, Assignee. Synthetic Layered MCM-56; its Synthesis and Use. United States Patent US 5,362,697, 1994 Nov 8.

[35] Igbari, O.; Xie, Y.; Jin, Z.; Liao, L. S., Microstructural and electrical properties of CuAlO₂ ceramic prepared by a novel solvent-free ester elimination process. *J. Alloys Compd.* **2015**, *653*, 219-27, DOI: 10.1016/ j.jallcom.2015.08.268.

[36] Khanmoradi, M.; Nikoorazm, M.; Ghorbani-Choghamarani. A., Anchoring of Cu(II)-vanillin Schiff base complex on MCM-41, A highly efficient and recyclable catalyst for synthesis of sulfides and 5-substituted 1H-tetrazoles and oxidation of sulfides to sulfoxides. *Appl. Organomet. Chem.* **2017**, 31, e3693, DOI: 10.1002/aoc.3693.

[37] Tang, G.; Li, M.; Wang, B.; Fang, Y.; Tan, T., Selective conversion of butanol into liquid branched olefins over zeolites. *Microporous Mesoporous Mater.* **2018**, *265*, 172-8, DOI: 10.1016/ j.micromeso.2018.02.017

[38] Dugkhuntod, P.; Imyen, T.; Wannapakdee, W.; Yutthalekha, T.; Salakhum, S.; *et al.*, Synthesis of hierarchical ZSM-12 nanolayers for levulinic acid esterification with ethanol to ethyl levulinate. *RSC Adv.* **2019**, *9*, 18087-97, DOI: 10.1039/C9RA03213D.

[39] Barrientos, E. J.; Lapuerta, M.; Boehman, A. L., Group additivity in soot formation for the example of C-5 oxygenated hydrocarbon fuels. *Combust. Flame.* **2013**, *160*, 1484-98, DOI: 10.1016/ j.combustflame.2013.02.024.

[40] Borders, J. R. C. L.; Handbook of Ultraviolet and Visible Absorption Spectra of Organic Compounds (Hirayama, Kenzo). ACS Publications, 1972.

[41] Klzilkilic, N; Schuchmann, H. P; Sonntag, C. V., The photolysis of tetrahydrofuran and of some of its methyl derivatives at 185 nm. *Can. J. Chem.* **1980**, *58*, 2819-2826, DOI: 10.1139/v80-452.

[42] Kamani, M.; Fazaeli, R.; Arjmand, M.; Ghorbani, M. H., Synthesis of CuO/MCM-41 photocatalyst nanocomposite; mechanistic study and optimization of quinoline oxidative degradation without auxiliary oxidant using response surface methodology. *Phys. Chem. Res.* **2020**, *8*, 175-202, DOI: 10.22036/ pcr.2019.201520.1676.

[43] Saadi, R.; Saadi, Z.; Fazaeli, R.; Fard, N. E., Monolayer and multilayer adsorption isotherm models for sorption from aqueous media. Korean. *J. Chem. Eng.* **2015**, *32*, 787-799, DOI: 10.1007/s11814-015-0053-7.